A&A 623, A128 (2019)
https://doi.org/10.1051/0004-6361/201834601

Astronomy & Astrophysics

Abundances and kinematics of carbon-enhanced metal-poor stars in the Galactic halo

A new classification scheme based on Sr and Ba[⋆,⋆⋆]

C. J. Hansen[1,2], T. T. Hansen[3], A. Koch[4], T. C. Beers[5], B. Nordström[2,6,7], V. M. Placco[5], and J. Andersen[2,6,7]

[1] Max Planck Institute for Astronomy, Königstuhl 17, 69117 Heidelberg, Germany
e-mail: hansen@mpia.de
[2] Copenhagen University, Dark Cosmology Centre, The Niels Bohr Institute, Vibenshuset, Lyngbyvej 2, 2100 Copenhagen, Denmark
[3] Mitchell Institute for Fundamental Physics and Astronomy and Department of Physics and Astronomy, Texas A&M University, College Station, TX 77843-4242, USA
[4] Zentrum für Astronomie der Universität Heidelberg, Astronomisches Rechen-Institut, Mönchhofstr. 12, 69120 Heidelberg, Germany
[5] Department of Physics and JINA Center for the Evolution of the Elements, University of Notre Dame, Notre Dame, IN 46556, USA
[6] Stellar Astrophysics Centre, Department of Physics and Astronomy, Aarhus University, Ny Munkegade 120, 8000 Aarhus C, Denmark
[7] Copenhagen University, The Cosmic Dawn Centre, The Niels Bohr Institute, Blegdamsvej 17, 2100 Copenhagen, Denmark

Received 7 November 2018 / Accepted 16 January 2019

ABSTRACT

Carbon-enhanced metal-poor (CEMP) stars span a wide range of stellar populations, from bona fide second-generation stars to later-forming stars that provide excellent probes of binary mass transfer and stellar evolution. Here we analyse 11 metal-poor stars (8 of which are new to the literature), and demonstrate that 10 are CEMP stars. Based on high signal-to-noise ratio (S/N) X-shooter spectra, we derive abundances of 20 elements (C, N, O, Na, Mg, Ca, Sc, Ti, Cr, Mn, Fe, Ni, Sr, Y, Ba, La, Ce, Pr, Nd, and Eu). From the high-S/N spectra, we were able to trace the chemical contribution of the rare earth elements (REE) from various possible production sites, finding a preference for metal-poor low-mass asymptotic giant branch (AGB) stars of 1.5 $M_{\odot}$ in CEMP-s stars, while CEMP-r/s stars may indicate a more massive AGB contribution (2–5 $M_{\odot}$). A contribution from the r-process – possibly from neutron star–neutron star mergers (NSM) – is also detectable in the REE stellar abundances, especially in the CEMP-r/s sub-group rich in both slow(s) and rapid(r) neutron-capture elements. Combining spectroscopic data with *Gaia* DR2 astrometric data provides a powerful chemodynamical tool for placing CEMP stars in the various Galactic components, and classifying CEMP stars into the four major elemental-abundance sub-groups, which are dictated by their neutron-capture element content. The derived orbital parameters indicate that all but one star in our sample (and the majority of the selected literature stars) belong to the Galactic halo. These stars exhibit a median orbital eccentricity of 0.7, and are found on both prograde and retrograde orbits. We find that the orbital parameters of CEMP-no and CEMP-s stars are remarkably similar in the 98 stars we study. A special case is the CEMP-no star HE 0020−1741, with very low Sr and Ba content, which possesses the most eccentric orbit among the stars in our sample, passing close to the Galactic centre. Finally, we propose an improved scheme to sub-classify the CEMP stars, making use of the Sr/Ba ratio, which can also be used to separate very metal-poor stars from CEMP stars. We explore the use of [Sr/Ba] versus [Ba/Fe] in 93 stars in the metallicity range $-4.2 \lesssim$ [Fe/H] < -2. We show that the Sr/Ba ratio can also be successfully used for distinguishing CEMP-s, CEMP-r/s, and CEMP-no stars. Additionally, the Sr/Ba ratio is found to be a powerful astro-nuclear indicator, since the metal-poor AGB stars exhibit very different Sr/Ba ratios compared to fast-rotating massive stars and NSM, and is also reasonably unbiased by NLTE and 3D corrections.

Key words. stars: abundances – stars: carbon – stars: kinematics and dynamics – stars: Population II – Galaxy: halo – nuclear reactions, nucleosynthesis, abundances

1. Introduction

Like many types of living organisms, most of the oldest, most-Fe-poor stars, are carbon rich. This indicates that C has been produced in large amounts, from the earliest times in the very first stars, right up until now. However, over time the dominant production sites may well have shifted. The demonstrated high frequency of carbon-enhanced metal-poor (CEMP) stars (up to 80% for [Fe/H] < –4, Yong et al. 2013; Placco et al. 2014; Yoon et al. 2018) seems to indicate that the first (likely massive) stars produced C, N, and O and possibly some Na and Mg, but not Fe or heavier elements in large amounts, keeping these stars Fe-poor.

To date, only two ultra-metal-poor ([Fe/H] < –4.5) stars without strong C enhancements have been identified (e.g.

⋆ Tables A1 and A2 are only available at the CDS via anonymous ftp to cdsarc.u-strasbg.fr (130.79.128.5) or via http://cdsarc.u-strasbg.fr/viz-bin/qcat?J/A+A/623/A128

⋆⋆ Based on observations obtained at ESO Paranal Observatory, programme 090.D-0321(A).

Caffau et al. 2011; Starkenburg et al. 2018). Most of the bona fide second-generation stars are CEMP-no stars, with low abundances of heavy elements on their surfaces (Yong et al. 2013), while the majority of CEMP stars remain those enhanced in slow neutron-capture elements; $\gtrsim$80% of these are known to be members of binary systems (Starkenburg et al. 2014; Hansen et al. 2016a). Two much-less populated sub-groups are the CEMP-r and CEMP-r/s stars, which are also enhanced in rapid neutron-capture material, making their stellar spectra extremely crowded at most wavelengths. Some refer to CEMP-r/s as CEMP-i stars, as they appear to be enriched by the *i*ntermediate neutron-capture process (e.g. Abate et al. 2016; Hampel et al. 2016). Understanding how stars in the individual CEMP sub-groups become enriched in various elements provides important clues on their progenitor populations, their nucleosynthetic pathways, and their masses, which in turn can help constrain the initial mass function. Moreover, we can assess early binarity over a wide stellar mass range.

Many of the CEMP stars known today are faint and remote, and therefore they have been observed with larger telescopes with efficient, lower-resolution spectrographs, sufficient to derive accurate molecular abundances. However, offsets in atomic abundances might be introduced when comparing to abundances derived from high-resolution spectra of the same stars. Despite possible limitations in abundance accuracy owing to low-resolution spectra, a dichotomy in absolute C abundances has been shown to enable reliable separation of CEMP-no and CEMP-s stars in the A(C)-versus-[Fe/H] diagram (Rossi et al. 2005; Spite et al. 2013; Bonifacio et al. 2015; Hansen et al. 2015a, 2016b; Yoon et al. 2016).

Previous studies have suggested that the CEMP-no stars are typically associated with the outer halo, while the majority of CEMP-s stars reside in the inner halo (Carollo et al. 2012, 2014; Beers et al. 2017; Lee et al. 2017; Yoon et al. 2018), but such dissections have so far mainly been based on distance estimates. To date, no kinematic study of these subclasses has been carried out (for large samples). This is vital for tracking the orbital histories of these stars to look for possible associations in phase space that could indicate a common origin, and to accurately trace the stars to their proper birth environment. This is now possible due to the recent advent of *Gaia*'s second data release (DR2, Gaia Collaboration 2018), which underscores the need for additional observations of, in particular, relatively bright CEMP stars.

As shown by Hansen et al. (2015a), the CEMP-no stars, which may dominate the outer Galactic halo, are essentially single stars, while the CEMP-s stars are predominantly found in binary systems. This implies that the carbon in the CEMP-no stars was synthesised elsewhere, and was then implanted into the natal clouds of the very metal-poor stars of today. Realistic galaxy-formation models must take this enrichment process into account, whether the progenitors were fast-rotating massive stars (FRMS; Maeder & Meynet 2003; Hirschi 2007; Frischknecht et al. 2016; Choplin et al. 2016) or other first-generation stars that ended their lives as mixing and fallback supernovae (SNe).

Here we analyse a sample of metal-poor stars with different chemical enrichments and probe their kinematics to determine their membership in the inner- or outer-halo populations. Based on chemical abundances of only two heavy elements (Sr and Ba) we provide a new method for sub-classifying the CEMP stars. Moreover, we use their detailed chemical patterns to explore the nature and mass of some of the first (massive) stars that enriched these old CEMP stars.

The paper is organised as follows. Section 2 outlines the observations, Sect. 3 describes the stellar-parameter determination, Sect. 4 presents the derivation of stellar abundances, and Sect. 5 highlights our abundance results. Section 6 describes the use of the Sr/Ba ratio for discrimination of CEMP-s, CEMP-r/s, and CEMP-no stars and Sect. 7 details the kinematics derived using orbital parameters based on *Gaia* DR2. A brief summary of our conclusions is provided in Sect. 8.

2. Observations

Our programme sample was selected from the "Catalogue of carbon stars found in the Hamburg-ESO survey" (Christlieb et al. 2001) and the later studies by Placco et al. (2010, 2011); the likely most metal-poor stars (based on line indices calculated directly from the objective-prism spectra) were targeted. Except for one star, all stars turned out to be CEMP stars with [Fe/H] $<$ -2.0 and [C/Fe] $>$ 1.0. The 11 sample stars were observed between October 2012 and January 2013 with X-shooter/VLT (Vernet et al. 2011) using a nodding technique. The three arms UVB/VIS/NIS were used with slits widths of 1.0"/0.9"/0.9", resulting in resolving powers of $R \sim 5400/8900/5600$, respectively, and covering the wavelength range 300–2500 nm. Stellar coordinates, exposure times, and heliocentric radial velocities are provided in Table 1. The raw echelle spectra were reduced using the X-shooter pipeline v. 2.6.5; the 1D spectra were radial-velocity shifted, co-added, and normalised. The radial velocity of HE 0002–1037 was measured from the Mg triplet and other strong lines, and subsequently the spectrum was shifted to zero velocity. The resulting spectrum was then used as a template for cross correlation to determine the radial velocities of the other programme stars.

3. Stellar parameter measurements

We follow the same approach for deriving stellar parameters and abundances as applied in Hansen et al. (2016b, Paper I), in order to make the samples as homogeneous as possible. The temperatures are based on $V - Ks$ colours, and are computed using the empirical infrared flux method (IRFM) relations from Alonso et al. (1999), adopting the mean IRSA[1] "S & F" reddening (Schlafly & Finkbeiner 2011). The $E(B - V)$ was converted to $E(V-K)$ following Alonso et al. (1996), and the necessary filter system corrections adopted according to Alonso et al. (1998) and Bessell (2005) before using the IRFM. Gravities were determined by fitting Padova isochrones (D. Yong priv. comm.), and the microturbulence was calculated using the empirical relation developed for the *Gaia*-ESO Survey[2] (M. Bergemann priv. comm). As is generally the case in low- to medium-resolution spectra of CEMP stars, determining the metallicity ([Fe/H]) is very challenging, due to the fact that these stars are metal-poor and exhibit weak Fe lines, which can suffer from the severe line blends from molecular bands (and in some cases also heavy-element atomic lines).

We therefore carefully vetted Fe lines that were clean in high-resolution spectra, and only included the ones that were useful in the X-shooter spectra. The Fe lines employed are listed in Table 2. This resulted in the stellar-atmospheric parameters

[1] https://irsa.ipac.caltech.edu/applications/DUST/

[2] A public spectroscopic survey using the ESO facility FLAMES/VLT targeting $>10^5$ stars, https://www.gaia-eso.eu, Gilmore et al. (2012).

Table 1. Observation log for X-shooter data.

Stellar ID	RA (2000.0)	Dec (2000.0)	V (mag)	K (mag)	$E(B-V)$ (mag)	UBV (mag)	VIS (mag)	NIR (mag)	$RV_{\rm helio}$ (km s^{-1})
HE 0002–1037	00 05 23.0	−10 20 23.0	13.70	11.47	0.037	800	700	3x285	−21.9
HE 0020–1741	00 22 44.9	−17 24 28.0	12.89	10.48	0.021	600	500	3x220	121.0
HE 0039–2635	00 41 39.9	−26 18 54.0	12.18	10.00	0.010	300	200	2x180	−29.5
HE 0059–6540	01 01 18.0	−65 23 59.0	13.26	11.11	0.017	1130	1030	2x600	37.3
HE 0151–6007	01 53 36.5	−59 53 05.0	13.36	10.73	0.018	1130	1030	2x600	58.7
HE 0221–3218	02 23 56.9	−32 04 40.0	15.92	13.53	0.016	150	40	220	67.9
HE 0253–6024	02 55 06.5	−60 12 17.0	13.26	13.35	0.022	930	830	4x250	100.3
HE 0317–4705	03 18 45.1	−46 54 39.0	12.55	10.15	0.013	530	430	2x300	171.6
HE 2158–5134	22 01 30.7	−51 20 09.0	12.17	9.93	0.023	230	130	300	18.2
HE 2258–4427	22 01 30.7	−44 11 27.0	12.44	9.86	0.008	670	570	3x245	132.4
HE 2339–4240	23 41 40.8	−42 24 03.0	13.15	11.05	0.014	630	530	3x230	15.1

Table 2. Fe I and Fe II lines used for parameter determination.

λ (Å)	χ (eV)	log gf
4071.738	1.608	−0.022
4528.614	2.176	−0.822
4890.755	2.876	−0.430
5012.068	0.859	−2.642
5191.455	3.040	−0.550
5194.941	1.557	−2.090
5198.711	2.223	−2.140
5339.928	3.266	−0.680
5371.490	0.960	−1.645
5415.192	4.386	0.500
5197.577	3.230	−2.348
5234.625	3.220	−2.050
5276.002	3.199	−1.900

listed in Table 3; for comparison, in brackets we list the temperatures and gravities based on *Gaia* DR2 photometry and parallaxes (Gaia Collaboration 2018), respectively.

There is overall good agreement between our adopted temperature and gravity measurements and the *Gaia*-based ones. For most stars (8 out of 11 analysed in this work) our values agree with the *Gaia* estimates within 150 K and 0.3 dex for log$g$, respectively, while one star deviates in temperature by ∼300 K, and another one deviates in gravity by 0.5 dex. The uncertainties on the stellar parameters are indicated in Table 3.

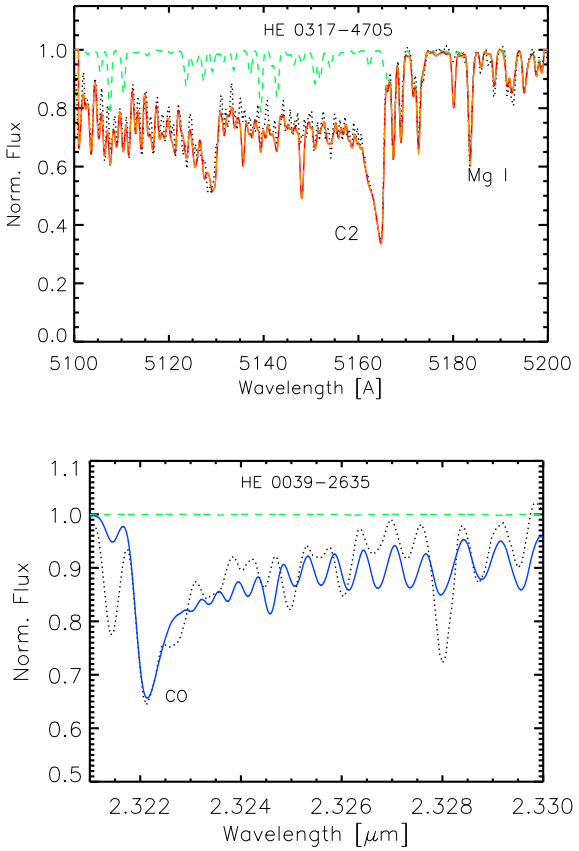

Fig. 1. *Top panel*: C_2 in HE 0317–4705 (green, no C_2; red [C/Fe] = 1.4). *Bottom panel*: CO in HE 0039–2635 (green, no CO; blue, [O/Fe] = 2.0).

4. Abundance analysis

Based on the derived stellar parameters, we interpolate ATLAS 9 atmospheric 1D models with new opacity distribution functions (Castelli et al. 2003). These, and a line list based on mainly Kurucz[3] and Sneden et al. (2016), were used together with MOOG (Sneden 1973, v. 2014) to derive stellar abundances via spectrum synthesis, assuming local thermodynamic equilibrium. We synthesise the CH, C_2, NH, CN, OH, and CO bands to obtain C, N, and O abundances, respectively (see Fig. 1) assuming molecular equilibrium. In most cases, the spectrum quality was too low to allow for a meaningful synthesis of OH (except for in a few stars with high S/N). Hence, the O abundances are therefore based on CO at 23 220 Å. When synthesising CN and CO bands, we use the already derived C abundances to derive N and O, respectively. The final abundances listed are based on an iterative process, which ceased when all C, N, and O bands were well-fit. Representative uncertainties on the abundances arising from uncertainties in the stellar parameters have been derived for HE 0059−6540 and are listed in Table 4.

Overall, there is a good agreement (∼0.2 dex) between the C abundances derived from CH and C_2 (see Table 5), and an even better agreement (0.1 dex) between the N abundance derived from NH and CN.

[3] http://kurucz.harvard.edu/linelists.html

Table 3. Our adopted stellar parameters compared to parameters from *Gaia* DR2 listed in parenthesis.

Stellar ID	$T_{\rm eff}$ (±100 K)	log g (±0.2 dex)	[Fe/H] (±0.1 dex)	ξ (±0.1 km s^{-1})
HE 0002–1037	5010 [4929]	2.0 [2.1]	−2.4	1.8
HE 0020–1741	4760 [4887]	1.3 [1.4]	−3.6	2.0
HE 0039–2635	4970 [4750]	1.9 [1.5]	−3.2	1.8
HE 0059–6540	5040 [4999]	2.1 [1.6]	−2.2	1.8
HE 0151–6007	4350 [4666]	1.0 [1.3]	−2.7	2.1
HE 0221–3218	4760 [4851]	2.5 [2.4]	−0.8	1.6
HE 0253–6024	4640 [4476]	1.2 [1.4]	−2.1	2.0
HE 0317–4705	4730 [4862]	1.3 [1.5]	−2.3	2.0
HE 2158–5134	4950 [4862]	1.9 [2.1]	−3.0	1.8
HE 2258–4427	4560 [4752]	1.0 [–]	−2.1	2.1
HE 2339–4240	5090 [5033]	2.3 [2.4]	−2.3	1.7

The oxygen abundances derived from OH may deviate by up to 0.3 dex, which we ascribe to the low S/N of the OH-band region in the UV and possible 3D effects (Dobrovolskas et al. 2013; Gallagher et al. 2016).

Abundances derived from our atomic line list (see Table A.1 - available at the CDS) are listed in Table 5. Here we targeted atomic lines of 16 species between Na and Eu that fall in regions that are as little affected by molecular bands as possible. Hence, we mainly focus on lines in the wavelength regions: 5200–5400 Å, 5800–5900 Å, 6100–6200 Å, and 6630–6680 Å. The abundances and results are described below.

5. Abundance results

Here we compare our results to those presented in Hansen et al. 2016b (Paper I). All of our sample stars are giants, and therefore there is a chance that they have reached an evolutionary stage at which internal mixing processes have taken place, and altered their original composition. We therefore checked their C/N ratios, following the approach in Spite et al. (2005). Figure 2 shows that all of our stars have [C/N] > −0.6 and are unmixed, while two stars (HE 0221-3218 with [C/N] = −0.3 and HE 0020–1741 with [C/N] = −0.4 and a high O abundance) are on the verge of becoming mixed. This does not affect our results, as HE 0221–3218 is the most metal-rich star that does not fall into the CEMP class. We note that the CEMP-no star (HE 0020–1741), with [C/N] = −0.4, is close to the mixing boundary in Fig. 2; it has a larger ^{13}C fraction than most of our other stars, and a very high oxygen abundance as well. This star is an evolved giant, but not yet at a point where we consider its surface composition to have been significantly altered. The isotopic abundance ratio for HE 0059–6540 exhibits a relatively large ^{13}C/^{12}C, however its atomic abundances seem to counter this, and with a gravity higher than that of HE 0020–1741, we do not consider HE 0059–6540 to be self-polluted. However, we remain cautious due to the ^{13}C/^{12}C isotopic ratio of this star.

Hence, when comparing to yield predictions that might trace the source that produced the elemental abundances locked up in these CEMP giants, we assert that all our programme CEMP stars are not significantly affected by stellar-evolution processes such as gravitational settling, levitation, and other mixing processes.

Based on the classification criteria listed in Beers & Christlieb (2005), with updates from Aoki et al. (2007), we find

Table 4. Uncertainties (σ) on derived abundances arising from the uncertainty on each of the stellar parameters which are added in quadrature to obtain the total uncertainty for HE 0059−6540.

Element	$\sigma(T_{\rm eff})$ (±100 K)	σ(log g) (±0.2 dex)	σ([Fe/H]) (±0.1 dex)	$\sigma(\xi)$ (±0.1 km s^{-1})	$\sigma_{\rm Total}$
CH	0.10	0.10	0.05	0.05	0.16
C_2	0.07	0.03	0.05	0.00	0.09
NH	0.20	0.15	0.10	0.05	0.27
CN	0.10	0.10	0.10	0.05	0.18
CO	0.20	0.10	0.05	0.05	0.23
Na	0.10	0.07	0.06	0.09	0.16
Mg	0.15	0.07	0.10	0.03	0.20
Ca	0.05	0.05	0.05	0.05	0.10
Sc	0.02	0.05	0.08	0.03	0.10
Ti	0.05	0.00	0.10	0.03	0.12
Cr	0.13	0.04	0.10	0.05	0.18
Mn	0.35	0.10	0.20	0.10	0.43
Ni	0.15	0.02	0.10	0.00	0.18
Sr	0.15	0.03	0.12	0.00	0.19
Y	0.11	0.02	0.10	0.04	0.16
Ba	0.05	0.05	0.05	0.08	0.12
La	0.05	0.03	0.07	0.03	0.10
Ce	0.12	0.08	0.15	0.13	0.25
Pr	0.08	0.02	0.10	0.06	0.14
Nd	0.05	0.04	0.09	0.03	0.11
Eu	0.02	0.05	0.10	0.05	0.12

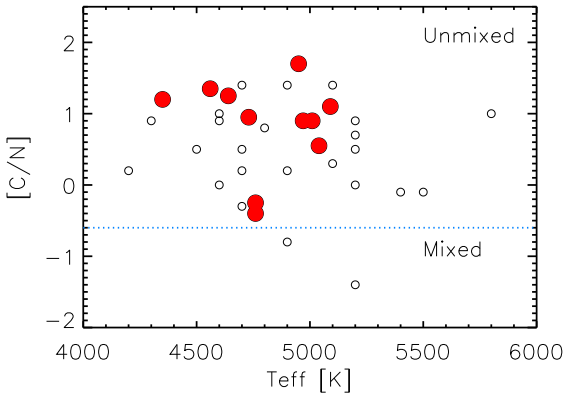

Fig. 2. Surface temperature vs. [C/N] ratio in this sample (filled, red circles) compared to that from Paper I (open circles).

that our sample contains one CEMP-no star (HE 0020–1741), five CEMP-*s* stars (HE 0039–2635, HE 0253–6024, HE 2158–5134, HE 2258–4427, HE 2339–4240), and four CEMP-*r*/*s* stars (HE 0002–1037, HE 0059–6540, HE 0151–6007, and HE 0317–4705). The CEMP-*s* star HE 2258–4427 is however on the verge of being classified a CEMP-*r*/*s* star. Finally, we have one metal-poor, but non-C-enhanced star (HE 0221–3218). Our results and their sub-classifications can be seen in Fig. 3 and Table 6.

Previous studies have used various elements or element pairs to sub-classify CEMP stars either into the four main classes or sub-groups thereof. In Masseron et al. (2010), the [Ba/C] ratio produced a linear trend as a function of [Fe/H] for CEMP-*s* stars but not for CEMP-*r*/*s* stars. However, Fig. 4 shows that the Ba/C ratio alone cannot separate CEMP-*s* from the CEMP-*r*/*s* stars. More recently, Yoon et al. (2016) split the CEMP-no stars into two sub-groups (their Group II and Group III stars), where, *A*(C), Mg, and Na were used as tracers. In Fig. 4, we explore whether

Table 5. Abundances from atomic lines, molecular bands, and isotopic ratios.

[X/Fe]	HE 0002–1037	HE 0020–1741	HE 0039–2635	HE 0059–6540	HE 0151–6007	HE 0221–3218
[Fe/H]	−2.4	−3.6	−3.2	−2.2	−2.7	−0.8
$^{13}C/^{12}C$	4/96	25/75	6/94	50/50	...	...
CH	1.9	1.5	2.7	1.3	1.4	0.1
C_2	1.9	...	2.8	1.4	1.7	0.1
CN	1.0	1.8	1.8	1.2	...	...
NH	1.0	1.9	1.8	0.8	0.2	0.4
O	1.1	2.3	2.0	1.3	0.5	0.4
NaI	<0.7	...	...	0.4	0.2	0.8
MgI	0.5	1.4	0.6	0.2	0.6	0.4
CaI	0.3	0.4	0.6	0.2	0.4	0.3
ScII	0.3	0.5	...	0.2	<0.5	0.5
TiI	0.5	0.4	0.7	0.5	0.5	0.4
CrI	−0.3	−0.1	0.0	−0.2	−0.4	0.1
MnI	−0.5	−0.4	...	−0.5	...	<0.4
NiI	0.1	0.1	0.1	−0.1	−0.2	0.3
SrII	<1.0	−0.1	1.6	1.2	1.1	0.3
YII	0.4	...	0.7	0.4	0.8	−0.1
BaII	2.0	−1.2	2.1	1.7	2.3	0.0
LaII	2.0	...	2.5	1.6	2.5	...
CeII	1.7	...	2.1	1.4	2.4	...
PrII	2.1	...	2.6	1.4	2.6	...
NdII	2.1	...	2.3	1.7	2.6	...
EuII	1.7	...	...	1.5	2.3	...
	HE 0253–6024	HE 0317–4705	HE 2158–5134	HE 2258–4427	HE 2339–4240	
[Fe/H]	−2.1	−2.3	−3.0	−2.1	−2.3	
$^{13}C/^{12}C$	5/95	6/94	4/96	5/95	5/95	
CH	1.3	1.4	2.6	1.4	1.7	
C_2	1.3	1.4	2.6	1.3	1.8	
CN	0.2	0.4	0.8	−0.1	0.6	
NH	0.0	0.5	0.9	0.0	0.6	
O	...	0.6	1.4	0.2	1.1	
NaI	<1.0	>−0.2	...	...	0.3	
MgI	0.2	0.5	0.8	0.2	0.4	
CaI	0.4	0.3	0.3	0.3	0.4	
ScII	0.1	−0.2	0.6	...	−0.2	
TiI	0.2	0.3	0.5	0.1	0.4	
CrI	−0.5	0.0	−0.1	−0.3	−0.3	
MnI	<0.4	<−0.9	...	<0.5	<0.5	
NiI	...	<−0.1	...	0.1	...	
SrII	1.5	1.7	2.6	1.7	1.6	
YII	0.8	0.6	1.8	1.0	0.8	
BaII	1.7	1.0	2.3	1.3	2.0	
LaII	1.5	1.4	<2.0	1.4	2.0	
CeII	1.2	1.5	<2.2	1.6	1.7	
PrII	1.0	1.4	2.6	1.4	2.0	
NdII	2.0	1.3	1.8	1.5	2.0	
EuII	<1.0	<1.0	...	0.8	...	

or not involving Mg in addition to Ba/C aids in the separation of CEMP-no, CEMP-*s*, and -*r*/*s* stars. As seen from Fig. 4, the combination of C, Mg, and Ba does not lead to a clear differentiation between the groups.

Based on their cosmological models, Hartwig et al. (2018) suggested that [Mg/C] could be used to tell if a second-generation star was enriched by a single event (mono-enriched) or was the result of several pollution events (multi-enriched).

The bottom panel of Fig. 4 shows our programme data compared to Yoon et al. (2016), where some of their CEMP-no Gr.III stars appear to be mono-enriched, while others lie below the predicted 3σ confidence level. Surprisingly, some of the CEMP-*s* stars also seem to be mono-enriched, while our CEMP-no star (HE 0020–1741) at first glance appears to be multi-enriched already at the low metallicity of [Fe/H] = −3.6. However, we note that this star has a very high Mg abundance, and the cosmological predictions are likely not able to deal with or represent peculiar enhancements. Additional observations of CEMP stars would be interesting to help clarify the situation, as well as the inclusion of

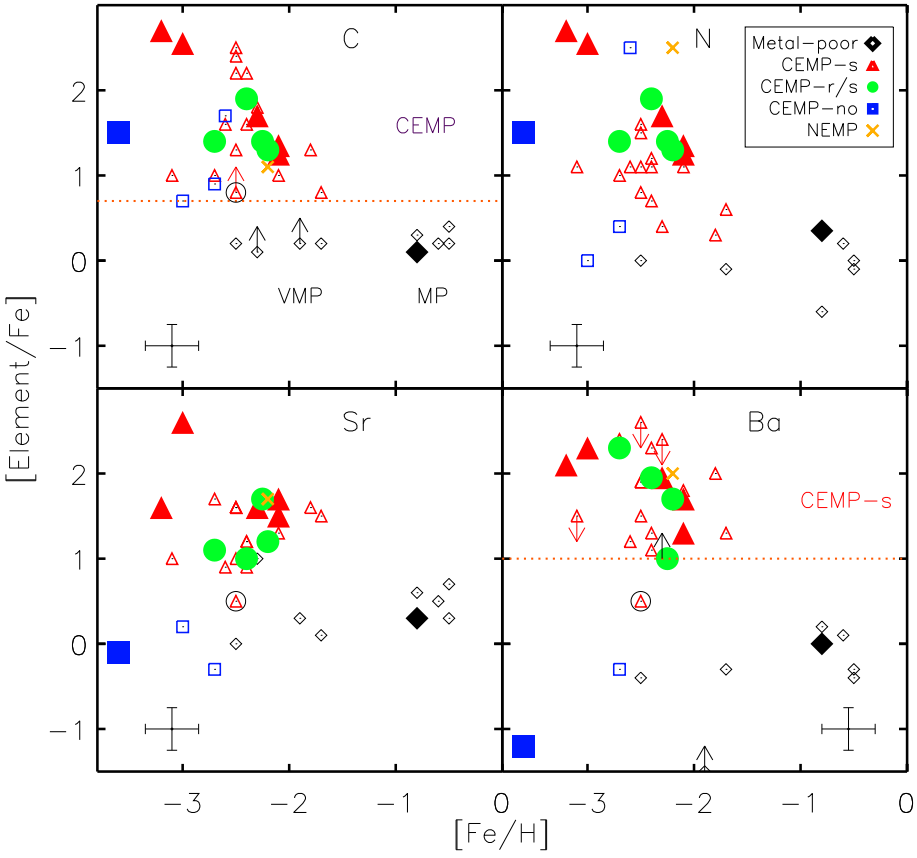

Fig. 3. C, N, Sr, and Ba abundances of our programme stars (filled symbols) compared to those in Paper I (open symbols).

different formation sites in the cosmological models. Binarity may also cloud the enrichment assessment (Arentsen et al. 2019).

Carbon has already been shown to be a good separator between CEMP-no and CEMP-*s* stars, but currently there is no consistent way of sub-classifying all CEMP stars into their respective groups. A separation of CEMP-*s* and CEMP−*r*/*s* stars was attempted in Hollek et al. (2015) using [Y/Ba]; however, their application was limited to these two groups, and was shown not to apply to all CEMP groups.

In Paper I, a separation based only on heavy elements such as Sr and Ba was also suggested to sub-classify the CEMP stars, and at the same time learn about their progenitor site. The Sr/Ba ratio is different in AGB stars and FRMS, which makes Sr/Ba an efficient and useful descriptor to trace possible formation sources in the sense that only two elements/absorption features need to be analysed to derive this abundance ratio. Additionally, Choplin et al. (2017) showed that the Sr/Ba ratio, together with the O production in FRMS, is much higher than in AGB stars.

Here we show that Sr and Ba can be used to separate not only the various sub-groups of CEMP stars but also to distinguish C-normal stars from CEMP stars. Moreover, Sr is intrinsically a much stronger absorption feature than Y, and from a nucleosynthetic perspective, they both most likely originate from the same formation process. The elements Sr and Ba exhibit strong absorption lines, and are therefore detectable in lower-resolution, low-S/N spectra, making them useful features for large surveys. By comparison, Y and Eu are much weaker, and tend to disappear in stellar spectra around [Fe/H] = −3 (see, e.g. Hansen et al. 2014a).

Among the stars in the programme sample, the Sr/Ba ratio appears to be a very informative quantity. A very high [Sr/Ba] = 1.1 is found for our CEMP-no star (HE 0020–1741), which is in fair agreement with the FRMS yields (see Fig. 5). We note that this ratio is almost as high as the record high value found in the Sgr dSph galaxy (Hansen et al. 2018); only two stars in François et al. (2007) exceed [Sr/Ba] = 1.0. We note that those studies focussed on C-normal stars, hence the ratios and formation sites may differ. On the other hand, a low [Sr/Ba] is found in CEMP-*r*/*s* stars (Abate et al. 2016; Hampel et al. 2016), and we propose that [Sr/Ba] > −0.5 could be used to separate CEMP-*s* from CEMP-*r*/*s* stars, in instances for which Eu cannot be detected in the spectra (see the discussion below for more details).

Keeping the small sample size in mind (11 stars), our findings indicate that FRMS provide a good representation of the CEMP-no stars, and to a smaller extent some CEMP-*s* stars (see Fig. 5). Moreover, in Fig. 5 we show [Sr/Ba] versus relative C and O abundances compared to generalised FRMS yields (Frischknecht et al. 2012) with an average of [Sr/Ba] ∼0.5 and AGB yields ([Sr/Ba] ∼−0.5 from predictions of metal-poor AGB stars with 1.5–2 $M_{\odot}$; Cristallo et al. 2011). The bottom panel of the same figure shows the separation of FRMS using O predictions from Choplin et al. (2017), contrasting with the above-described AGB yields. Despite some of the stars falling slightly off the predictions, there is an overall good agreement between the results illustrated by the two panels.

The match of FRMS yields to CEMP-*s* abundances was also shown in Choplin et al. (2017) for seemingly single CEMP-*s* stars, indicating that a sub-group of CEMP-*s* stars could be polluted by fast-rotating massive stars. However, according to the simulations by Abate et al. (2018) all CEMP-*s* stars could be undetected binaries with periods > 10^4 days. The vast majority of CEMP-*s* stars (which are binaries) are well-reproduced by AGB stars. We discuss their mass range below.

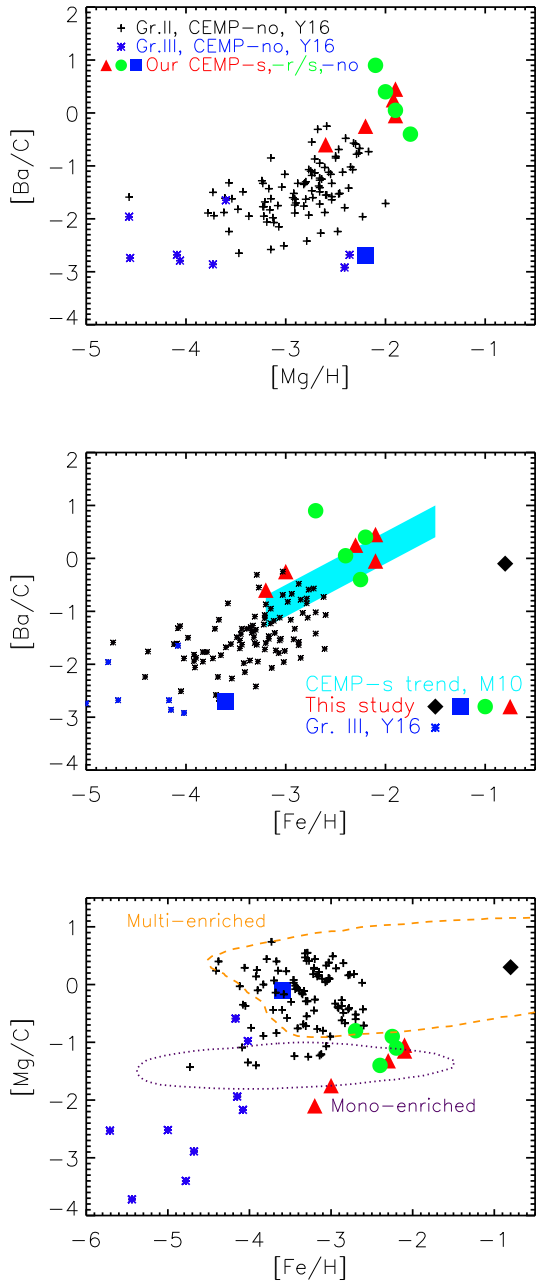

Fig. 4. *Top panel*: ratio of [Ba/C] as a function of [Fe/H] and [Mg/H], for our programme data compared to literature studies (Yoon et al. 2016, Y16). The *middle panel* shows that our CEMP-*s* and CEMP-*r*/*s* stars both fall in the CEMP-*s* region proposed by Masseron et al. (2010, M10). *Bottom panel*: two different enrichment regions in a [Mg/C] vs. [Fe/H] diagnostics figure. In all panels we show our CEMP-no stars as filled blue squares, CEMP-*s* stars as filled red triangles, CEMP-*r*/*s* as green circles, and C-normal metal-poor stars as filled black diamonds.

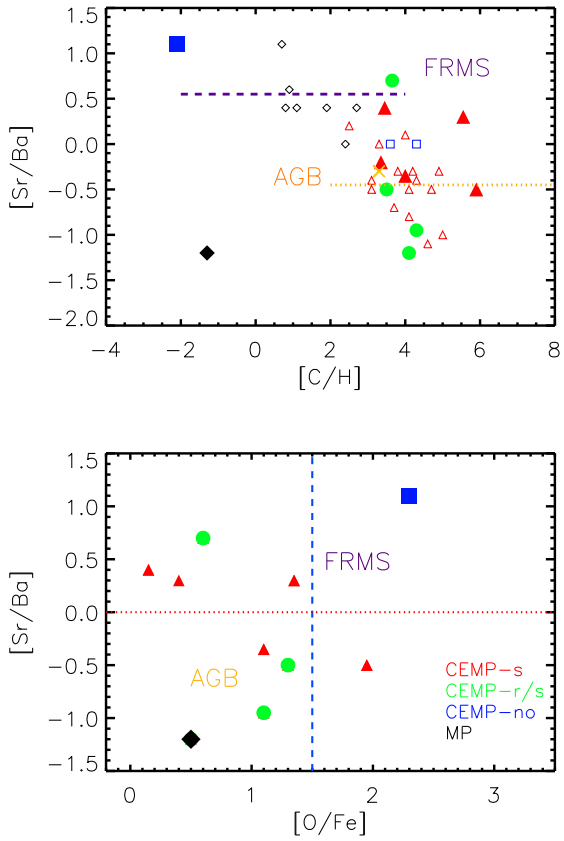

Fig. 5. *Top panel*: [C/H] vs. [Ba/Sr] for the sample stars compared to the sample from Paper I. *Bottom panel*: [Sr/Ba], as a function of [O/Fe], for stars considered in this paper.

The best way to explore the origin of various CEMP subgroups is still their detailed abundance patterns, from which masses of the AGB donor star, as well as contributions from AGB stars, SNe, and neutron star mergers can be extracted.

For comparison to the yields (Fig. 6), we limit our consideration to the four likely mono-enriched stars. Here we have compared to the most metal-poor AGB yields from Lugaro et al. (2012), which have a total metallicity ([Fe/H]) of ∼−2.2. The magneto-hydrodynamical jet-driven supernova (MHD jet-SNe) yields are from Winteler et al. (2012), and finally, the dynamical ejecta from a neutron star merger (consisting of two neutron stars of 1.0 $M_{\odot}$ each) are shown as well (Korobkin et al. 2012 and Rosswog et al. 2013). We acknowledge that this is an incomplete representation of possible NSM yields.

Based on χ^2 fitting of the rare earth elements (REEs), we find that the majority of our CEMP-*s* stars fit the metal-poor, low-mass AGB yields from Lugaro et al. (2012) with 1.5 $M_{\odot}$, with a few stars slightly preferring 2.0 $M_{\odot}$. Our best fits typically result in $\chi^2 \sim 1.01-1.07$. The CEMP-*r*/*s* stars seem to favour the slightly more massive AGB donors with 2.0−5.0 $M_{\odot}$, where low-mass NSMs appear to have contributed to the REEs ($56 < Z < 63$), while the rare MHD core-collapse SNe may have enriched these stars in the lighter elements Sr and Y (see Fig. 6). We note that NSM disc ejecta could also have contributed material rich in Sr and Y, instead of or in addition to MHD jet-SNe.

6. A new classification scheme based on Sr and Ba

As already proposed in Paper I, the Sr/Ba ratio might be interesting for use in chemical tagging, since these elements are formed in different nucleosynthesis processes and astrophysical sites. Strontium is made in larger amounts than Ba in FRMS via the (weak) *s*-process. In contrast, the typical low-mass AGB star produces more Ba than Sr, yielding a low Sr/Ba ratio, while more massive AGB stars produce slightly larger, or equal amounts of Sr compared to Ba. This is the case for the metal-poor AGB yields from Lugaro et al. (2012), in agreement with Cristallo et al. (2011). The exact details and abundances vary depending on the metallicity of the model, as the AGB *s*-process yields are secondary, and hence metallicity (seed) dependent. Based on the Lugaro et al. models and our CEMP measured [Sr/Ba] values, we propose a CEMP sub-classification based on the Sr/Ba

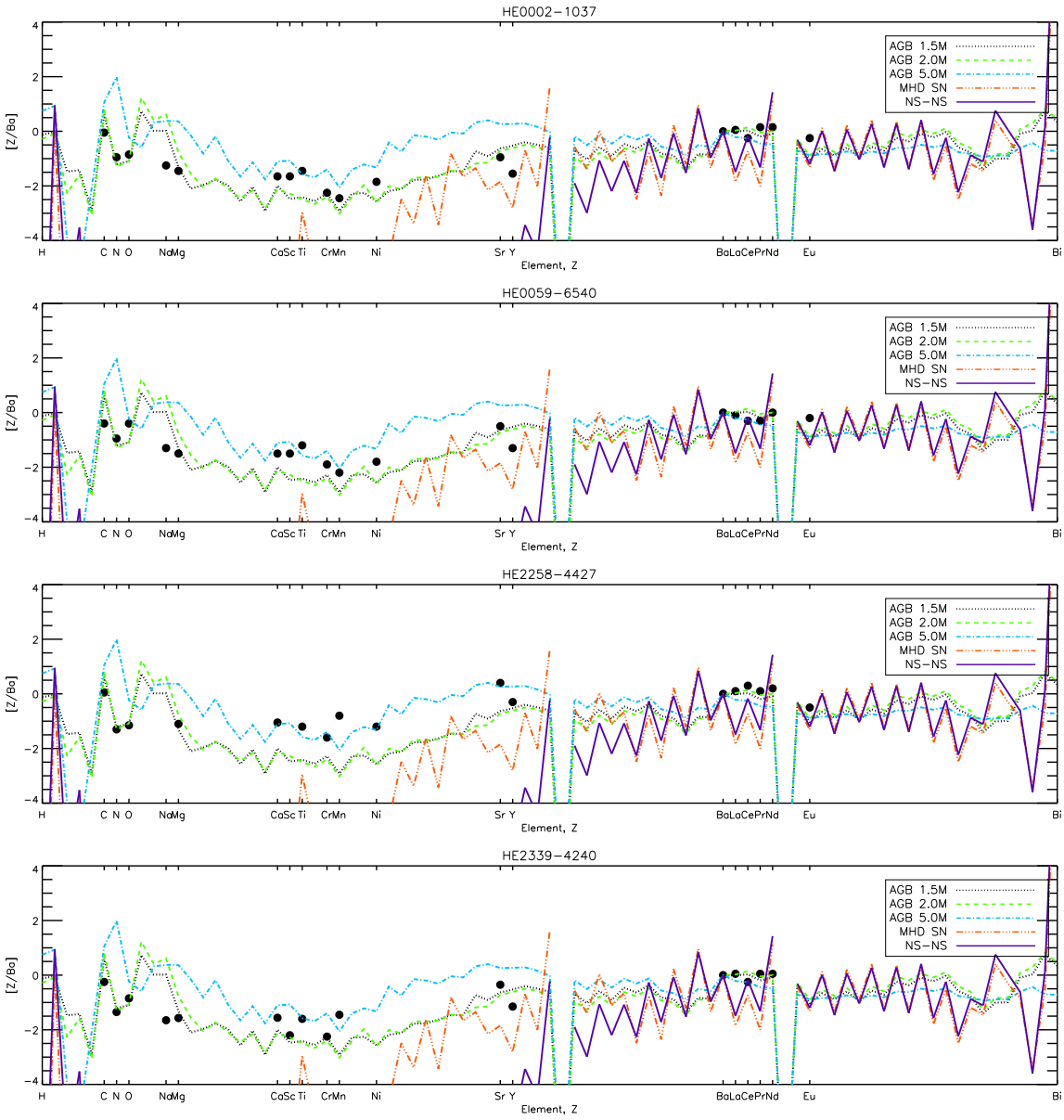

Fig. 6. Yields from AGB stars (masses 1.5, 2.0, and 5 $M_{\odot}$, Z = 0.0001/ [Fe/H] = −2.3; Lugaro et al.), MDH jet-SNe (Winteler et al. 2012), and NSMs (Korobkin et al. 2012; Rosswog et al. 2013), compared to the CEMP-r/s stars (HE 0002−1037, HE 0059−6540) and CEMP-s stars (HE 2158−5134, HE 2339−4240), which should all be mono-enriched. Yields and stellar abundances have been scaled to match the Ba abundance of the star shown in the respective panels.

ratio as listed in Table 6. The asterisk identifies stars where the old classification scheme, based on values in Table 5 following Beers & Christlieb (2005), and the new proposed Sr/Ba classification do not agree.

Right at the level of [Sr/Ba] = 0.5 a few stars may be misclassified however. Besides those, only one star (HE 0317–4705) would be incorrectly assigned as a CEMP-s instead of r/s. The lower bound on the CEMP-r/s class is set based on currently known [Sr/Ba] ratios and the MHD jet-SNe yield prediction (in order to separate it from CEMP-r stars, which are presently few in number, and not believed to be the product of AGB mass transfer). While the yields from Lugaro et al. (2012) cannot fully explain the CEMP-r/s stars, their light-to-heavy s-process ratio is seen to typically fall below −0.5 in their Fig. 7. When applying this to the CEMP sample in Paper I, all CEMP stars are well-classified, except for two CEMP-s stars, HE 0448–4806 and HE 2235–5055, for which Eu in our previous study could not be measured owing to low S/Ns, rendering the testing of the class challenging. These latter two stars are, according to this classification, CEMP-r/s stars. Clearly, this must be tested in a much larger sample; however, being able to sub-classify CEMP stars accurately, and to directly tie a site and its progenitor mass by only measuring abundances of two heavy elements, seems promising in the era of large surveys. Strontium and barium are the only two heavy elements beyond Fe that exhibit readily detectable absorption features in low-/moderate-resolution, low S/N spectra (Caffau et al. 2011; Hansen et al. 2013, 2015b, 2016b).

An additional advantage of using Sr and Ba is their robust behaviour in LTE versus NLTE. Several studies have shown that the Sr II NLTE corrections are on average only ±0.1 dex (Bergemann et al. 2012; Hansen et al. 2013), and that they may only in a few cases increase to 0.2 dex, depending on stellar parameters and the Sr line used (Andrievsky et al. 2011). The Ba NLTE corrections are slightly higher (±0.1 − 0.3 dex), again

Table 6. [Sr/Ba] from our sample and yield predictions. Below the CEMP sub-classification based on Beers & Christlieb (2005) and Table 4.

Star/Model	[Sr/Ba]	This study Old (new)
HE 0002–1037	−0.95	CEMP-r/s (r/s)
HE 0020–1741	1.10	CEMP-no (no)
HE 0039–2635	−0.50	CEMP-s (r/s)*
HE 0059–6540	−0.50	CEMP-r/s (r/s)
HE 0151–6007	−1.20	CEMP-r/s (r/s)
HE 0221–3218	0.30	MP (MP)
HE 0253–6024	−0.20	CEMP-s (s)
HE 0317–4705	0.70	CEMP-r/s (s)*
HE 2158–5134	0.30	CEMP-s (s)
HE 2258–4427	0.40	CEMP-s (s)
HE 2339–4240	−0.35	CEMP-s (s)
MHD SN	−1.80	W12[a]
1.5 AGB	−0.63	L12[b]
2.0 AGB	−0.72	L12
5.0 AGB	0.26	L12
CEMP-no	[Sr/Ba] > 0.75	New classification
CEMP-s	−0.5 < [Sr/Ba] < 0.75	New classification
CEMP-r/s	−1.5 < [Sr/Ba] < −0.5	New classification
CEMP-r	[Sr/Ba] < −1.5	New classification
MP	[Sr/Ba] < 0.75 & [Ba/Fe] < 0	New classification

Notes. "*" indicates cases where our new classification disagrees with the old one. [(a)]W12: Yields from Winteler et al. (2012) [(b)]L12: Non-Solar-scaled data from Table 3 and 4 from Lugaro et al. (2012) taken from the end of the AGB evolution.

depending on the stellar parameters (Andrievsky et al. 2009; Korotin et al. 2015). Taking HE 2158–5134 as an example (T/logg/[Fe/H]: ∼ 5000/2.0/ − 3), the Sr NLTE correction would be −0.05 to −0.1 dex, according to Andrievsky et al. (2011) and Hansen et al. (2013), and the NLTE Ba abundance should be increased by 0.1 dex for the 5853 Å line (Andrievsky et al. 2009). This means that the Sr/Ba ratio would at most change by ±0.2 dex in NLTE versus LTE, which is in agreement with the metal-poor Sr/Ba NLTE study of C-normal stars by Andrievsky et al. (2011). A test of the 3D corrections for Sr indicated that the NLTE and 3D corrections would cancel out (Hansen et al. 2014b), which likely would bring the 1D LTE values closer to the fully 3D, NLTE-corrected Sr/Ba ratios. This makes this ratio a stable segregator that not only allows us to classify stars for statistical studies, but also provides information on the nature of the progenitors.

In comparison, C abundances are prone to large 3D corrections (on the order of −0.3 to −0.6 dex, especially the CEMP-no stars with lower absolute A(C)); they may also be biased by the lack of exact O abundances (Dobrovolskas et al. 2013; Gallagher et al. 2016, 2017). This correction could ultimately push some CEMP-no stars out of the CEMP class, owing to the lowered (3D) C abundance. Oxygen is more difficult to derive than C, and is therefore missing for many CEMP stars, leaving an incomplete picture of the nature of the stars and their actual abundances. This could influence the fraction of metal-poor stars that are classified as CEMP stars.

Using Ba and Sr to sub-classify the CEMP stars, we note some separation from simple inspection of Fig. 7. The metal-poor, C-normal sample from François et al. (2007) was NLTE corrected by Andrievsky et al. (2011), and these abundances (offset by a minor amount compared to our LTE values), clearly populate a distinct region of the diagram, despite overlapping perfectly in [Fe/H] with our CEMP sample (which ranges from [Fe/H] = −2 down

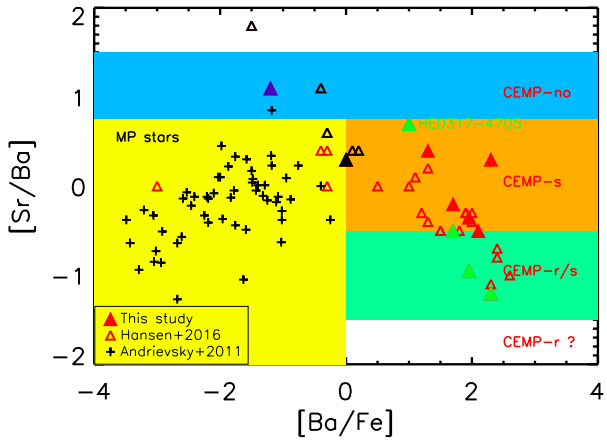

Fig. 7. [Sr/Ba] vs. [Ba/Fe] from this study compared to Hansen et al. (2016b, Paper I) and NLTE values (+) from Andrievsky et al. (2011). The blue symbol colour indicates CEMP-no stars, red CEMP-s, and green CEMP-r/s, while black (yellow region) shows C-normal metal-poor stars. Our suggested sub-classifications are highlighted in similar colours to the symbols.

to ∼−4). Except for one CEMP-s/no star (HE 0516–2515), the C-normal metal-poor region is cleanly separated from the CEMP stars. The cut may have to be adjusted in a larger sample, however, all CEMP stars appear to have higher [Ba/Fe] than C-normal stars, regardless of their sub-classes. The division at [Ba/Fe] = 0 is loosely set, and spreads around these values in agreement with an average Galactic chemical evolution value based on observations from Hansen et al. (2012) and Roederer et al. (2014). The blue CEMP-no panel is poorly populated, and would need more data points to confirm the bounds of this region. Here, C abundances may be crucial to separate a star with low Ba and normal C abundances from a CEMP-no star. The most metal-poor CEMP-no stars (with [Fe/H] < −4) may be viewed with caution, as these could fall slightly below the suggested cut (see Yong et al. 2013). Except for one CEMP-r/s star (HE 0317–4705), the CEMP-s region is cleanly separated, and shows a strong overlap with the CEMP-s stars in Caffau et al. (2018), while the CEMP-r/s region is more contaminated by CEMP-s stars.

Additional i-process yields could help narrow this down. If the i-process is solely associated with AGB stars, and sets in at neutron densities that are only an order of magnitude larger than the classical AGB s-process (Karakas & Lattanzio 2014; Abate et al. 2016), some overlap between these two groups would be expected. These considerations are based on small number statistics, and the cuts between the CEMP classes need to be confirmed for a larger sample. The Sr/Ba ratio, however, clearly provides useful information about the nature of the individual stars and their progenitors, and helps us to understand the large star-to-star scatter seen both in LTE and NLTE-corrected samples (Andrievsky et al. 2011; Hansen et al. 2013).

The Sr/Ba ratio is also interesting from a purely nucleosynthetic point of view. Several studies have proposed that Sr could be formed by both a heavy and light process (e.g. a main and a weak process), while Ba, located beyond the second s-process peak, would mainly be formed by a main process (Qian & Wasserburg 2008; Andrievsky et al. 2011; Hansen et al. 2014a). Moreover, with the abundance Sr being much higher than that of Ba, a second or additional process or contribution appears to be required (François et al. 2007). This is in good agreement with Hansen et al. (2014a), where the abundance patterns in all but one of the most metal-poor stars could be well-explained

by two neutron-capture processes contributing to the abundances derived for very metal-poor stars (with [Fe/H] $\lesssim -2.5$).

The most complete nucleosynthetic mapping still requires a rich abundance pattern, which in turn calls for either high-S/N, moderate-resolution spectra or high-resolution spectra. A note of caution when comparing abundances derived from spectra of various quality and resolution should be made. Several studies have dealt with both high- and moderate-resolution spectra and have found differences in abundances derived from these when analysing the same stars (Caffau et al. 2011; Cohen et al. 2013; Aguado et al. 2016). When comparing our abundances to those derived in for example Placco et al. (2016) for HE 0020–1741, we found that the [Fe/H] and other abundances differ by 0.3–0.4 dex, mainly due to (unresolved) blends. However, by using our list of clean Fe lines, this difference can be reduced. Alternatively, it might be worth reducing the stellar metallicities derived from moderate-resolution metal-poor spectra if their abundances are to be compared to those with high-resolution metallicities.

7. Kinematic analysis

In order to investigate the orbital histories of CEMP stars, we first cross-identified their coordinates with the second data release (DR2) of *Gaia* (Gaia Collaboration 2018), which yielded the required five-parameter astrometric solution in terms of position, proper motions, and parallaxes. The latter were considered in terms of the prior-free, Bayesian distance estimates of Bailer-Jones et al. (2018), in turn derived from the *Gaia* parallaxes (to avoid, e.g. negative parallaxes). Using the radial velocities derived above, we backwards-integrated the stellar orbits for 12 Gyr in a Galactic potential accounting for a logarithmic halo and spherical bulge (Fellhauer et al. 2008) and a disc model by Dehnen & Binney (1998). This neglects the warp and flare of the outer disc (e.g. Momany et al. 2006), which will have little impact on our distant stars.

For comparison purposes, we also performed the analysis in an identical matter for the CEMP-no, CEMP-*s*, and metal-poor stars from the studies of Hansen et al. (2015c, 2016a,b,c). Here, we note an overlap of three objects from our sample with the latter comparison samples, which naturally led to the same cross-match with *Gaia*. Accordingly, we found the same orbital parameters from the two data sets, except for slight modifications due to small differences in the adopted radial velocity[4] between either study (of 10 km s^{-1} at most). For the entire sample of 98 stars, 89% have relative parallax errors ($\sigma_{\overline{\omega}}/\overline{\omega}$) below 40%, two thirds are better determined than 12%, and the median relative distance uncertainty, σ_d/d, amounts to 12%.

Figure 8 shows the resulting orbital parameters for our present sample and the comparison stars, namely peri- and apocentre distances (R_{peri}, R_{apo}), maximum height above the plane (Z_{max}), and orbital eccentricity (e).

We also computed the total specific orbital energy (i.e. kinetic plus Galactic potential energy) and the specific orbital angular momentum, which we specify here in terms of the azimuthal action $L_z = -J_\varphi$.

As L_z is a conserved quantity in axisymmetric potentials, its combination with the orbital energy (also a constant) in the Lindblad diagram of Fig. 9 offers an opportunity to identify groups of stars in phase space that are otherwise seemingly uncorrelated on the sky (Gómez et al. 2010). This proves particularly valuable

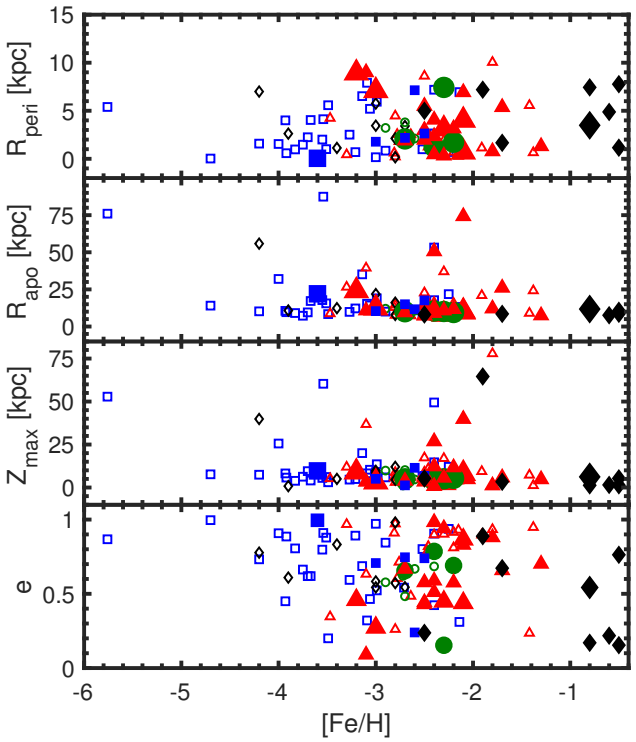

Fig. 8. Derived orbital parameters of the present and comparison samples, separated by the chemical sub-groups. Here, CEMP-no stars are shown as blue squares, CEMP-*s* as red triangles, CEMP-*r* and -*r*/*s* as green circles, and C-normal stars as black diamonds. Large, filled symbols are data from this work, while small filled symbols refer to the sample of Hansen et al. (2016b). Finally, the comparison stars of Hansen et al. (2015c, 2016c,a) are indicated as open symbols following the same colour code as in Figs. 3–5.

if groups of stars are to be associated with an accretion origin from disrupted satellites (e.g. Roederer et al. 2018). As an in-situ population of stars in binaries, the CEMP-*s* stars are unlikely to exhibit any correlations, and indeed no obvious clumping in Fig. 9 is seen. The same holds for the CEMP-no stars, arguing in favour of them originating from early, proto-halo enrichment phases without any coherent orbital histories. All of the stars are bound to the Milky Way, as their orbital energies are less than zero.

Finally, Fig. 10 shows a Toomre diagram, displaying the Galactocentric rotation velocity, V, and its perpendicular component, $T = \sqrt{U^2 + W^2}$. In this representation, an orbit is defined as retrograde for $V < 0$. This diagram is an often-used diagnostics tool to kinematically separate the Galactic components (e.g. Bensby et al. 2003), which we can use here to efficiently single out halo stars (see also Bonaca et al. 2017; Koppelman et al. 2018; Posti et al. 2018; Veljanoski et al. 2019).

Here, we adopted the criterion of Koppelman et al. (2018) to identify bona fide halo stars as $|v - v_{LSR}| > 210$ km s^{-1}, where v designates the total velocity of the star, and v_{LSR} refers to the local standard of rest, which we adopt here as 232 km s^{-1} with a solar peculiar motion of $(U, V, W)_\odot = (11.1, 12.24, 7.25)$ km s^{-1} (Schönrich et al. 2010). This renders 70% of the entire sample halo stars (including our present work and the reference sets), while only 4 out of 11 of the stars from the current work would qualify as halo progeny via this strict criterion. Kordopatis et al. (2013) asserted that the low-metallicity tail of the metal-weak thick disc extends down to [Fe/H] = −2, while the stars in the (C)EMP samples at velocities between 100 and 210 km s^{-1} with

[4] We note a typographical error in Table 2 of Hansen et al. (2016c) for the star HE 0020–1741, which, according to the radial velocity table in their appendix, should be listed as 93.04 ± 0.07 km s^{-1}.

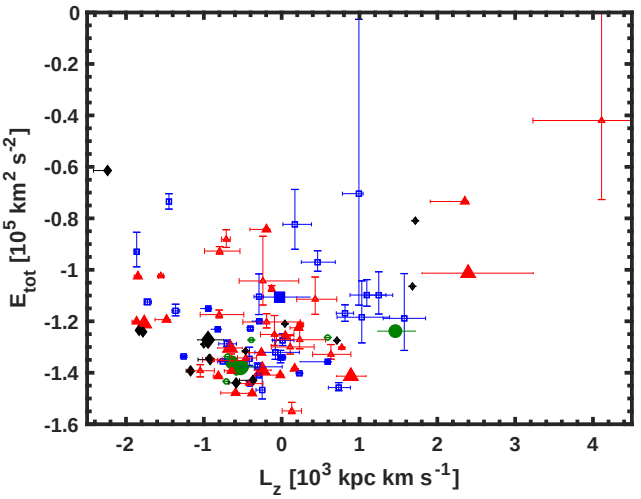

Fig. 9. Lindblad diagram for the same stars as in the previous figures.

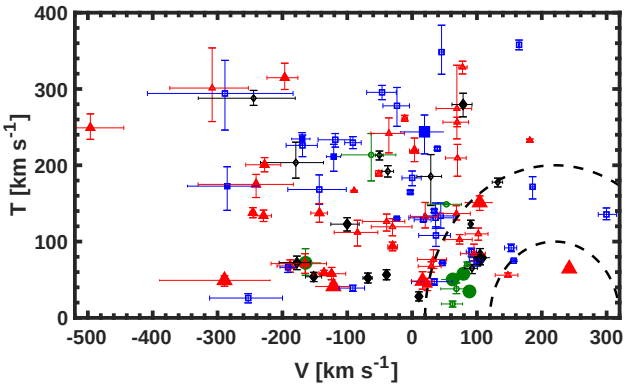

Fig. 10. Toomre diagram using the same symbols as in Fig. 8. The dashed circles indicate a 3D space velocity relative to the local standard of rest of 100 and 200 km s^{-1}, respectively, centred on $V_{\rm LSR}$ = 232 km s^{-1}.

reliable distances ($\sigma_{\overline{\omega}}/\overline{\omega}$ < 13%) ranging from [Fe/H] = −2.2 to −3.9 are more likely to be halo stars. Moreover, only two of those stars (HE 0507−1430 and LP 624–44) lie in the range 1 kpc < $Z_{\rm max}$ < 2 kpc (see Table A.2, available at the CDS). It is therefore likely that those metal-poor stars with disc-like orbits are either captured halo objects or could constitute an overlapping, inner-halo component, as their apocentres are also typically within ∼12 kpc. As for the sub-groups, there is a marginal preponderance of CEMP-*s* stars (9/26) at these velocities, while the other CEMP sub-classes are roughly represented in equal parts in the (kinematic) thick disc/halo transition.

In order to investigate the origin and properties of the various classes of metal-poor stars, Table 7 lists the fractions of stars in each class satisfying certain orbital and kinematic constraints.

The median heliocentric distance of the entire sample (98 stars) and the stars of the present study (11 stars) are 3.4 and 4.4 kpc, respectively. It is worth noting that the entire sample of 98 stars, as well as each CEMP sub-class in itself, is kinematically unbiased with regards to the U and W components, with approximately half the stars moving on prograde or retrograde orbits. The CEMP-*r* and -*r*/*s* stars appear to have a slightly larger contribution of positive velocities, but this group also contains the lowest number of stars (10% of the sample), as manifested in the larger (Poisson) errors on their fractions, which holds for most of the arguments below. Likewise, there is a balance of prograde and retrograde motions, and the full sample displays only mild net rotation at a mean < V >= −23 ± 13 km s^{-1} and a velocity dispersion of 128 ± 10 km s^{-1}. The same holds when considering the CEMP sub-groups, albeit with a smaller dispersion (75 ± 20 km s^{-1}) for the CEMP-*r*, −*r*/*s* stars. The values of these dispersions are also listed in Table 7. Overall, these values are broadly consistent with the kinematic properties of the Milky Way halo (e.g. Battaglia et al. 2005). From this aspect we can conclude that our entire sample is kinematically uncorrelated and is an in situ halo population, rather than a major, accreted component that would lead to rotation signatures (Deason et al. 2011). However, given the possible biases in target selection and overall sample size, these results should not be over-interpreted.

The majority of stars have eccentric orbits, with e in excess of 0.5, and the median eccentricity of our sample is 0.7, which confirms their membership in the halo. It is noteworthy that the most eccentric orbits are found among the C-normal, extremely metal-poor stars. About 60% of the stars are inhabitants of the inner halo, if we place the inner/outer halo transition via the stars' apocentres within ∼15 kpc (Carollo et al. 2010). This fraction is mostly independent on the CEMP sub-group, although we note that all of the CEMP-*r* and -*r*/*s* stars populate these inner regions. In turn, approximately one in four stars reaches apocentre distances exceeding 20 kpc regardless of CEMP sub-group, bringing them into the outer-halo regions. The metal-poor ([Fe/H] = −1.8) star HE 0854+0151 appears to have an apocentre of 290 kpc, which would place it outside the virial radius of the Galaxy. The orbital period is accordingly long, at ∼5 Gyr. This object has originally been classified as a CEMP-*s* star by Hansen et al. (2016a). Strictly, its more metal-rich nature defies this classification, along with three more candidates above [Fe/H] = −2 from that list. These should thus rather be labelled CH-stars – or a new, more stringent classification should be adopted. Despite their fundamentally different enrichment channels and purported origins (e.g. Bonifacio et al. 2015), the mean orbital parameters of CEMP-*s* and CEMP-no stars are, on average, remarkably similar.

In the following, we address a few cases with distinct kinematics.

HE 2158−5134. This newly analysed CEMP-*s* star, with a low metallicity of [Fe/H] = −3, exhibits the lowest velocity of the entire sample, at 68 ± 3 km s^{-1} relative to the LSR. Further, it has a moderate eccentricity (0.27) and a height above the plane, $Z_{\rm max}$, of 3 kpc. Kinematically, it may be a captured halo object or related to the metal-weak thick disc, despite its very low metallicity. Two additional CEMP-*s* and CEMP-no stars (HE 2238–4131 and HE 1300+0157) exhibit disc-like kinematics, if we take a velocity cut at 100 km s^{-1} as a discriminant.

Metal-rich stars. Five stars (HE 0408–1733, HE 2138–1616, HE 2141–1441, HE 2357–2718, and HE 0221-3218) have metallicities in the range −0.8 < [Fe/H] < −0.5, and thus are at the high-metallicity tail of the halo's metallicity distribution (Schörck et al. 2009). They exhibit a variety of orbital parameters, with reliable distance estimates to better than <38%, which are consistent with a halo origin, although we note that the perpendicular velocity component, T, is overall small and does not exceed 100 km s^{-1} (see Table A.2). It is feasible that these stars formed in the Galactic disc or bulge and were subsequently ejected.

High-velocity stars. Several stars in our sample have total velocities relative to the LSR exceeding 500 km s^{-1}. While some of them are hampered by larger parallax errors (on the order of 25–45%), the objects with the largest motions (HE 0854+0151 and HE 0058–3449) have distance estimates that are precise to better than 16%. These objects, with the highest values of

Table 7. Statistics of orbital parameters for each of the CEMP sub-groups.

Property	CEMP-no	CEMP-s	CEMP-r, r/s	C-normal
Fraction of total sample	0.34	0.41	0.09	0.16
$U < 0\,\mathrm{km\,s^{-1}}$	0.58 ± 0.03	0.47 ± 0.03	0.33 ± 0.12	0.62 ± 0.07
$V < 0\,\mathrm{km\,s^{-1}}$	0.45 ± 0.03	0.55 ± 0.03	0.22 ± 0.11	0.56 ± 0.07
$W < 0\,\mathrm{km\,s^{-1}}$	0.45 ± 0.03	0.50 ± 0.03	0.33 ± 0.12	0.44 ± 0.07
$e > 0.5$	0.79 ± 0.04	0.70 ± 0.03	0.78 ± 0.14	0.75 ± 0.08
$R_{\mathrm{apo}} < 13\,\mathrm{kpc}$	0.45 ± 0.03	0.60 ± 0.03	1.00 ± 0.16	0.75 ± 0.08
$R_{\mathrm{apo}} > 20\,\mathrm{kpc}$	0.21 ± 0.03	0.28 ± 0.03	...	0.19 ± 0.06
$R_{\mathrm{peri}} < 3\,\mathrm{kpc}$	0.64 ± 0.04	0.60 ± 0.03	0.67 ± 0.13	0.38 ± 0.07
$v_{\mathrm{LSR}} < 100\,\mathrm{kpc}$	0.03 ± 0.03	0.05 ± 0.03	...	...
$v_{\mathrm{LSR}} > 300\,\mathrm{kpc}$	0.48 ± 0.03	0.55 ± 0.03	0.22 ± 0.11	0.50 ± 0.07
$\sigma_V\,(\mathrm{km\,s^{-1}})$	127 ± 17	142 ± 17	75 ± 20	103 ± 20
$\langle R_{\mathrm{apo}} \rangle$ (kpc)	14.1	12.2	10.1	11.2
$\langle R_{\mathrm{peri}} \rangle$ (kpc)	2.2	2.2	2.1	3.5
$\langle Z_{\mathrm{max}} \rangle$ (kpc)	7.5	5.9	5.1	5.1
$\langle e \rangle$	0.74	0.68	0.66	0.58

Notes. The fractions listed within each sub-group satisfy the given kinematic condition and median values for the parameters. Error bars are solely based on Poisson statistics.

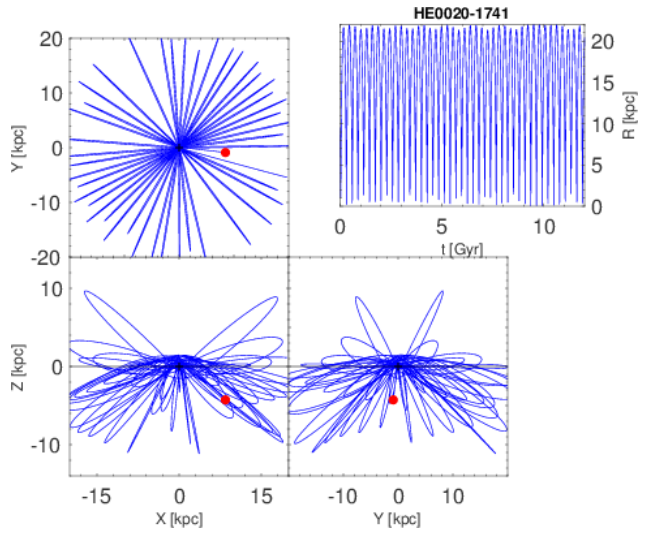

Fig. 11. Orbital projections of the CEMP-no star HE 0020−1741, the object with the most eccentric orbit of our sample ($e = 0.99$). Combined with its abundances and overall kinematics, in particular a large Z_{max}, an accretion origin of this star cannot be excluded.

608 and 757 km s^{-1}, are metal-poor CH- and CEMP-s stars, at [Fe/H] = −1.8 and −2.0, respectively, which is fully in-line with the recent detections of metal-poor hyper-velocity stars in *Gaia* DR2 (Hawkins & Wyse 2018).

Close pericentres. About 10% of our sample have pericentric distances closer than 500 pc (Table A.2). Here, we highlight the CEMP-no star HE 0020–1741, with a large apocentric distance of 22 kpc. Despite a distance uncertainty of 25%, it has the most eccentric orbit of our sample $e = 0.99$, which brings it to a close Galactocentric passage, within ∼53 pc, and a period of ∼550 Myr (see Fig. 11). While we cannot unambiguously constrain its origin in the central Galactic regions, it is worth noting that the oldest and therefore possibly most metal-poor stars are believed to have formed in the innermost ($R_{\mathrm{GC}} \lesssim 3.5$ kpc) halo regions (Brook et al. 2007; Tumlinson 2010), and in fact progressively more CEMP stars are being found toward these central parts of the Milky Way (Koch et al. 2016). Also noteworthy is the large height of this star above the plane, $Z_{\mathrm{max}} = 10$ kpc. This could also indicate that this star was once accreted into the Milky Way halo. This alternative scenario is further bolstered by its chemical composition (Table 4), which shows signatures of enrichment by faint SNe, as often seen in low-mass environments such as the dwarf spheroidal galaxies (Skúladóttir et al. 2015; Susmitha et al. 2017).

8. Conclusion

While the absolute C abundance, A(C), may provide a rough classification of CEMP stars into two groups (CEMP-s and CEMP-no), measured abundances of heavy elements beyond Fe are needed to better understand their origin and formation sites. In particular, if we want to know the mass of the associated AGB star or constrain the r-process site, a more complete abundance pattern is needed. The Sr/Ba ratio appears to be a good discriminant, and we suggest values and regions to sub-classify CEMP-no, CEMP-r/s, and CEMP-s stars. The exact cuts may need to be adjusted based on a larger sample.

Here we show that the careful analysis of moderate-resolution, high-S/N spectra provides precise and accurate abundance information to within ∼0.2 dex for 20 elements (including Fe) and two isotopes (^{12}C and ^{13}C). It is remarkable that moderate-resolution X-shooter data provide abundances that are sufficient in number and accuracy for exploring this class of metal-poor C-enriched stars. Compared to Paper I, we also showed that a $S/N > 40$ (at 4000 Å) is needed to obtain information on O and a number of heavy elements. Careful selection of Fe lines is crucial in order not to overestimate the [Fe/H] in moderate-resolution CEMP spectra. For this purpose, we provide a vetted line list. Alternatively, reducing the [Fe/H] by ∼0.3−0.4 dex from previously published lower-resolution spectra would be an option, if they are to be compared with high-resolution ones. This might be important both now and in the future when comparing data across various high- and lower-resolution surveys.

A comparison to yield predictions showed that FRMS can reproduce our CEMP-no and a few (single) CEMP-s or

CEMP-r/s stars, while the majority of these are binary stars enhanced directly by an AGB companion star. A sub-division of the CEMP-s and CEMP-r/s stars may be made (based on small number statistics), in that low-mass ($\sim$1.5 $M_{\odot}$) AGB stars appear to lead to CEMP-s stars, while CEMP-r/s stars could be enriched by more massive AGB stars ($\sim$2$-$5 $M_{\odot}$). This could mean that early binary systems may favour low-mass AGB companions (in agreement with Abate et al. 2018). However, this is still speculative, and requires testing with a larger CEMP sample.

Our chemodynamical results indicate that all but two stars in the sample of 98 objects considered here belong to the halo populations, and that the CEMP-s and CEMP-no stars have remarkably similar kinematics. With the current *Gaia* DR2 data, they cannot easily be assigned to the inner/outer halo, as the properties of the CEMP-no and CEMP-s are only marginally different, but we estimate that 25% of the stars (CEMP and C-normal) reach the outer halo. With our sample alone we cannot confirm that the CEMP-no stars mainly belong to the outer halo, while CEMP-s stars dominate the inner halo (as proposed in Carollo et al. 2012). Most of the CEMP stars (this study, Paper I and literature CEMP studies) have an eccentricity of 0.7. The extremely metal-poor CEMP-no star, HE 0020–1741, stands out by having the most eccentric orbit with a close Galactocentric passage.

The moderate-resolution, high-S/N X-shooter spectra have again proved their worth in stellar and Galactic spectroscopy – not only for very distant AGNs or GRBs, for which the instrument was designed. Combined with *Gaia* data, these spectra are very powerful in the analysis and classification of CEMP stars and in tracing their origins.

Acknowledgements. CJH acknowledges support from the Max Planck Society. CJH and AK acknowledge support from the Collaborative Research Centre SFB 881 "The MW System" (Heidelberg University, subprojects A05 and A08) of the German Research Foundation (DFG). TCB and VMP acknowledge partial support from grant PHY 14-30152; Physics Frontier Center / JINA Center for the Evolution of the Elements (JINA-CEE), awarded by the US National Science Foundation.

References

Abate, C., Stancliffe, R. J., & Liu, Z.-W. 2016, A&A, 587, A50
Abate, C., Pols, O. R., & Stancliffe, R. J. 2018, A&A, 620, A63
Aguado, D. S., Allende Prieto, C., González Hernández, J. I., et al. 2016, A&A, 593, A10
Alonso, A., Arribas, S., & Martinez-Roger, C. 1996, A&AS, 117, 227
Alonso, A., Arribas, S., & Martinez-Roger, C. 1998, A&AS, 131, 209
Alonso, A., Arribas, S., & Martínez-Roger, C. 1999, A&AS, 140, 261
Andrievsky, S. M., Spite, M., Korotin, S. A., et al. 2009, A&A, 494, 1083
Andrievsky, S. M., Spite, F., Korotin, S. A., et al. 2011, A&A, 530, A105
Aoki, W., Beers, T. C., Christlieb, N., et al. 2007, ApJ, 655, 492
Arentsen, A., Starkenburg, E., Shetrone, M. D., et al. 2019, A&A, 621, A108
Bailer-Jones, C. A. L., Rybizki, J., Fouesneau, M., Mantelet, G., & Andrae, R. 2018, AJ, 156, 58
Battaglia, G., Helmi, A., Morrison, H., et al. 2005, MNRAS, 364, 433
Beers, T. C., & Christlieb, N. 2005, ARA&A, 43, 531
Beers, T. C., Placco, V. M., Carollo, D., et al. 2017, ApJ, 835, 81
Bensby, T., Feltzing, S., & Lundström, I. 2003, A&A, 410, 527
Bergemann, M., Hansen, C. J., Bautista, M., & Ruchti, G. 2012, A&A, 546, A90
Bessell, M. S. 2005, ARA&A, 43, 293
Bonaca, A., Conroy, C., Wetzel, A., Hopkins, P. F., & Kereš, D. 2017, ApJ, 845, 101
Bonifacio, P., Caffau, E., Spite, M., et al. 2015, A&A, 579, A28
Brook, C. B., Kawata, D., Scannapieco, E., Martel, H., & Gibson, B. K. 2007, ApJ, 661, 10
Caffau, E., Bonifacio, P., François, P., et al. 2011, Nature, 477, 67
Caffau, E., Gallagher, A. J., Bonifacio, P., et al. 2018, A&A, 614, A68
Carollo, D., Beers, T. C., Chiba, M., et al. 2010, ApJ, 712, 692
Carollo, D., Beers, T. C., Bovy, J., et al. 2012, ApJ, 744, 195
Carollo, D., Freeman, K., Beers, T. C., et al. 2014, ApJ, 788, 180
Castelli, F., & Kurucz, R. L. 2003, IAU Symp., 210, 20P
Choplin, A., Maeder, A., Meynet, G., & Chiappini, C. 2016, A&A, 593, A36
Choplin, A., Hirschi, R., Meynet, G., & Ekström, S. 2017, A&A, 607, L3
Christlieb, N., Green, P. J., Wisotzki, L., & Reimers, D. 2001, A&A, 375, 366
Cohen, J. G., Christlieb, N., Thompson, I., et al. 2013, ApJ, 778, 56
Cristallo, S., Piersanti, L., Straniero, O., et al. 2011, ApJS, 197, 17
Deason, A. J., Belokurov, V., & Evans, N. W. 2011, MNRAS, 411, 1480
Dehnen, W., & Binney, J. 1998, MNRAS, 294, 429
Dobrovolskas, V., Kučinskas, A., Steffen, M., et al. 2013, A&A, 559, A102
Fellhauer, M., Wilkinson, M. I., Evans, N. W., et al. 2008, MNRAS, 385, 1095
François, P., Depagne, E., Hill, V., et al. 2007, A&A, 476, 935
Frischknecht, U., Hirschi, R., & Thielemann, F.-K. 2012, A&A, 538, L2
Frischknecht, U., Hirschi, R., Pignatari, M., et al. 2016, MNRAS, 456, 1803
Gaia Collaboration (Brown, A. G. A., et al.) 2018, A&A , 616, A1
Gallagher, A. J., Caffau, E., Bonifacio, P., et al. 2016, A&A, 593, A48
Gallagher, A. J., Caffau, E., Bonifacio, P., et al. 2017, A&A, 598, L10
Gilmore, G., Randich, S., Asplund, M., et al. 2012, The Messenger, 147, 25
Gómez, F. A., Helmi, A., Brown, A. G. A., & Li, Y.-S. 2010, MNRAS, 408, 935
Hampel, M., Stancliffe, R. J., Lugaro, M., & Meyer, B. S. 2016, ApJ, 831, 171
Hansen, C. J., Primas, F., Hartman, H., et al. 2012, A&A, 545, A31
Hansen, C. J., Bergemann, M., Cescutti, G., et al. 2013, A&A, 551, A57
Hansen, C. J., Montes, F., & Arcones, A. 2014a, ApJ, 797, 123
Hansen, C. J., Caffau, E., & Bergemann, M. 2014b, IAU Symp., 298, 409
Hansen, T., Hansen, C. J., Christlieb, N., et al. 2015a, ApJ, 807, 173
Hansen, C. J., Ludwig, H.-G., Seifert, W., et al. 2015b, Astron. Nachr., 336, 665
Hansen, T., Hansen, C. J., Christlieb, N., et al. 2015c, ApJ, 807, 173
Hansen, T. T., Andersen, J., Nordström, B., et al. 2016a, A&A, 588, A3
Hansen, C. J., Nordström, B., Hansen, T. T., et al. 2016b, A&A, 588, A37
Hansen, T. T., Andersen, J., Nordström, B., et al. 2016c, A&A, 586, A160
Hansen, C. J., El-Souri, M., Monaco, L., et al. 2018, ApJ, 855, 83
Hartwig, T., Yoshida, N., Magg, M., et al. 2018, MNRAS, 478, 1795
Hawkins, K., & Wyse, R. F. G. 2018, MNRAS, 481, 1028
Hirschi, R. 2007, A&A, 461, 571
Hollek, J. K., Frebel, A., Placco, V. M., et al. 2015, ApJ, 814, 121
Karakas, A. I., & Lattanzio, J. C. 2014, PASA, 31, e030
Koch, A., McWilliam, A., Preston, G. W., & Thompson, I. B. 2016, A&A, 587, A124
Koppelman, H., Helmi, A., & Veljanoski, J. 2018, ApJ, 860, L11
Kordopatis, G., Gilmore, G., Wyse, R. F. G., et al. 2013, MNRAS, 436, 3231
Korobkin, O., Rosswog, S., Arcones, A., & Winteler, C. 2012, MNRAS, 426, 1940
Korotin, S. A., Andrievsky, S. M., Hansen, C. J., et al. 2015, A&A, 581, A70
Lee, Y. S., Beers, T. C., Kim, Y. K., et al. 2017, ApJ, 836, 91
Lugaro, M., Karakas, A. I., Stancliffe, R. J., & Rijs, C. 2012, ApJ, 747, 2
Maeder, A., & Meynet, G. 2003, A&A, 411, 543
Masseron, T., Johnson, J. A., Plez, B., et al. 2010, A&A, 509, A93
Momany, Y., Zaggia, S., Gilmore, G., et al. 2006, A&A, 451, 515
Placco, V. M., Kennedy, C. R., Rossi, S., et al. 2010, AJ, 139, 1051
Placco, V. M., Kennedy, C. R., Beers, T. C., et al. 2011, AJ, 142, 188
Placco, V. M., Frebel, A., Beers, T. C., & Stancliffe, R. J. 2014, ApJ, 797, 21
Placco, V. M., Frebel, A., Beers, T. C., et al. 2016, ApJ, 833, 21
Posti, L., Helmi, A., Veljanoski, J., & Breddels, M. A. 2018, A&A, 615, A70
Qian, Y.-Z., & Wasserburg, G. J. 2008, ApJ, 687, 272
Roederer, I. U., Preston, G. W., Thompson, I. B., et al. 2014, AJ, 147, 136
Roederer, I. U., Hattori, K., & Valluri, M. 2018, AJ, 156, 179
Rossi, S., Beers, T. C., Sneden, C., et al. 2005, AJ, 130, 2804
Rosswog, S., Piran, T., & Nakar, E. 2013, MNRAS, 430, 2585
Schlafly, E. F., & Finkbeiner, D. P. 2011, ApJ, 737, 103
Schörck, T., Christlieb, N., Cohen, J. G., et al. 2009, A&A, 507, 817
Schönrich, R., Binney, J., & Dehnen, W. 2010, MNRAS, 403, 1829
Skúladóttir, Á., Tolstoy, E., Salvadori, S., et al. 2015, A&A, 574, A129
Sneden, C. A. 1973, PhD Thesis, The University of Texas at Austin, USA
Sneden, C., Cowan, J. J., Kobayashi, C., et al. 2016, ApJ, 817, 53
Spite, M., Cayrel, R., Plez, B., et al. 2005, A&A, 430, 655
Spite, M., Caffau, E., Bonifacio, P., et al. 2013, A&A, 552, A107
Starkenburg, E., Shetrone, M. D., McConnachie, A. W., & Venn, K. A. 2014, MNRAS, 441, 1217
Starkenburg, E., Aguado, D. S., Bonifacio, P., et al. 2018, MNRAS, 481, 3838
Susmitha, A., Koch, A., & Sivarani, T. 2017, A&A, 606, A112
Tumlinson, J. 2010, ApJ, 708, 1398
Veljanoski, J., Helmi, A., Breddels, M., & Posti, L. 2019, A&A, 621, A13
Vernet, J., Dekker, H., D'Odorico, S., et al. 2011, A&A, 536, A105
Winteler, C., Käppeli, R., Perego, A., et al. 2012, ApJ, 750, L22
Yong, D., Norris, J. E., Bessell, M. S., et al. 2013, ApJ, 762, 26
Yoon, J., Beers, T. C., Placco, V. M., et al. 2016, ApJ, 833, 20
Yoon, J., Beers, T. C., Dietz, S., et al. 2018, ApJ, 861, 146